Psyrras, N., Sextos, A., Crewe, A. J., Dietz, M., & Mylonakis, G. (2020). Physical modelling of the seismic response of gas pipelines in laterally in homogeneous soil. *Journal of Geotechnical and Geoenvironmental Engineering*, *146*(5). https://doi.org/10.1061/(ASCE)GT.1943-5606.0002242

Physical modelling of the seismic response of gas pipelines in laterally inhomogeneous soil

N. Psyrras[1]; A. Sextos[2], M. ASCE; A. Crewe[3]; M. Dietz[4]; G. Mylonakis[5], M. ASCE

Abstract: This paper reports on results from a series of 1-g, reduced-scale, shake table tests of a 216m-long portion of an onshore steel gas transmission pipeline embedded in horizontally layered soil. A set of first-order ~~set of~~ dynamic similitude laws was employed to scale system parameters appropriately. Two sands of different mean grain diameter and bulk density were used to assemble a compound symmetrical test soil consisting of three uniform blocks in a dense-loose-dense configuration. The sand-pipe interface friction coefficients were measured at 0.23 and 0.27. Modulated harmonic and recorded ground motions were applied as table excitation. To monitor the detailed longitudinal strain profiles in the model pipe, bare Fiber Bragg Grating cables were deployed. In most cases, the pipe response was predominantly axial while bending became significant at stronger excitation~~s~~. levels. Strain distributions displayed clear peaks at or near the block interfaces, in accord with numerical predictions, with magnitudes increasing at resonant frequencies and with excitation level. By extension to full-scale, peak axial strain amounted to approximately 10^{-3}, a demand half the yield strain, but not negligible given the low in-situ soil stiffness contrast and soil-pipe friction.

Author Keywords: gas pipelines, seismic excitation, inhomogeneous soil, shake table experiment

[1] Ph.D. Candidate, Dept. of Civil Engineering, University of Bristol
[2] Professor, Dept. of Civil Engineering, University of Bristol; M. ASCE
[3] Reader, Dept. of Civil Engineering, University of Bristol
[4] Research Fellow, Dept. of Civil Engineering, University of Bristol
[5] Professor, Dept. of Civil Engineering, University of Bristol; M. ASCE

Introduction

The vulnerability of long-span structures to differential earthquake-induced ground motion is a perennial topic of concern in engineering practice. Notably, attention is increasingly shifting towards ~~the~~ seismic protection of future-proof energy infrastructure assets like underground gas pipelines, reflecting the global transition to cleaner energy sources.

Gas transmission pipelines cross terrains ~~with~~ of variable morphology to move natural gas from wells to storage facilities, power plants and urban distribution networks. Typology data on this class of pipes can be sourced from Psyrras et al. (2019). Experience from past earthquakes suggests that damage inflicted to ~~the~~ transmission networks of this type can cause long service disruption and severe (often difficult-to-predict) socioeconomic losses. While the majority of pipeline damage reported to date is rightly attributed to permanent ground deformation (Chen et al. 2002; O'Rourke and Palmer 1996), there ~~exists~~ is sufficient field evidence to ~~support the claim~~ suggest that seismic wave propagation is also a source of damage (EQE Summary Report 1995; O'Rourke 2009; Sakurai and Takanashi 1969). Local buckling failures in steel pipelines have ~~often~~ been observed (Housner and Jennings 1972; O'Rourke and Liu 1999), in which cases localized curvatures and strains can become large and lead to non-linear collapse of the section, or even rupture and content leakage in the long run.

Pioneering works on soil-pipe interaction include those of Shinozuka and Koike (1979), Trautmann and O'Rourke (1985) and O'Rourke and Hmadi (1988). In a seminal effort, Hindy and Novak (1979) developed a matrix-based formulation of the dynamic equilibrium of a soil-pipe system to study the elastic response of pipelines to seismic excitation, both in homogeneous sites and in sites consisting of laterally ~~different~~ variable media. It was found that for body waves propagating along the pipeline, peak axial and bending stresses occur near the boundary of the two media, which are larger than those in homogeneous sites. Predictions also revealed that bending stresses due to S-waves are much smaller than the axial stresses due to P-waves. Nishio et al. (1980) and Nishio et al. (1983) conducted laboratory tests of buried pipelines in valley and cut-and-fill settings subject to horizontal base excitation. Analytical methods were used to study the strain response of buried pipelines laid through dipping soil layers (Akiyoshi and Fuchida 1988; Liu and O'Rourke 1997), cut-and-fill embankments (Ando et al.

1992), and multiple soil media (Liang 1995). Psyrras and Sextos (2017) present a comprehensive review on multiple aspects of seismic safety of pipelines, including recent advances in analysis and design methods. More recently, a series of studies reported on the buckling potential of gas pipelines buried in media with sharp stiffness transitions during seismic shaking (Psyrras et al. 2018, 2019a; Tsinidis et al. 2018); in these, non-linear finite element models were developed to analyze the factors that contribute to the development of localized deformation in the pipe walls leading to plastic buckling, and to describe the type of the resulting buckling response. Along the same vein, Yu et al. (2018) proposed elastic analytical solutions for the dynamic bending response of tunnel liners running through dissimilar soils due to harmonic shear waves and confirmed that demand in terms of internal forces increases with increasing stiffness contrast across different soil layers.

However, experimental verification of pipeline strain concentrations in zones of changing soil properties and the associated consequences for pipeline structural integrity, as predicted in the above references, is quite limited. This is understood in light of the spatially extended character of the problem and the difficulty in scaling down ~~it~~ the prototype systems into manageable dimensions to test in the laboratory ~~of~~ with acceptable fidelity. This study is a contribution towards the lab-scale physical modelling of dynamic axial soil-pipeline interaction in the case of a gas transmission pipeline running through laterally non-homogeneous cohesionless soil, subjected to vertically propagating shear waves. The test platform combined the 3m-by-3m shake table and the 5-m-long Equivalent Shear Beam soil chamber (referred to as ESB hereafter) of the Earthquake and Large Structures (EQUALS) Laboratory at the University of Bristol. The specific objectives of the test campaign were to

- physically model the actual dynamic soil-pipe interaction (SPI) effects in the presence of lateral gradients in soil properties;
- measure the magnitude and distribution of the induced axial and bending strains along the pipe;
- compare the experimental results with theoretical predictions;
- infer the possibility of plastic buckling failure at prototype scale;
- ~~elucidate~~ explore the role of the interface Coefficient of Friction (COF) as a mitigating factor.

This work aims at developing through new experimental data know how on the mechanisms of axial SPI in laterally inhomogeneous soil and its effects on high-pressure gas pipelines in seismically active areas. The experimental setup used is briefly discussed in Psyrras et al. (2019b) and is elaborated here.

Experimental setup

Laboratory equipment

This study used the earthquake simulator at the EQUALS Laboratory at University of Bristol (Fig. 1a). The shake table comprises a 3m×3m cast aluminum platform powered by 8 hydraulic actuators and is able to excite all 6 DOFs simultaneously. Each actuator has a dynamic capacity of 70 kN and a maximum stroke of 300 mm. The platform has a maximum payload of 15 Mg and is laid inside an isolated reinforced concrete block weighing 300 Mg. The table can attain maximum horizontal accelerations of 1.6g at 10 t payload, with operational frequencies in the range 0-100 Hz~~,~~ depending on the dead load.

To hold the test soil in place, the ESB developed by Crewe et al. (1995) was used. This apparatus is one of a series of similar devices built in the ’90s at the University of Bristol to enable physical modelling of geotechnical systems under seismic shaking (Fig. 1b and c). The ESB is made of eleven RHS aluminum rings, stacked alternately with soft rubber blocks to create a flexible hollow box measuring 4.8m×1.2m×1.0m (L×H×W). Its relatively large size makes it an ideal candidate for pipeline testing in an earthquake lab. Its floor is roughened with a thin sand layer to maximize shear wave transmission; the internal end walls (in the short direction) are similarly treated, while the internal side-walls (in the long direction) are lubricated to better approximate plane strain conditions. Rigid steel-restraining frames support the side walls on a system of bearings to prevent undesirable motion in the transverse direction. Designed to provide minimum resistance to shearing, the ESB allows the test soil to drive the horizontal motion, while it offers minimum inertia thanks to its low weight, and sufficient soil

confinement for geostatic conditions to develop. When empty, its natural frequency has been measured at 3.5 Hz.

Soil profiles and properties

To adequately reproduce the free field boundary conditions at the ESB ends, the same geomaterial should be used in the vicinity of both end-walls to ensure the best possible coupling between the compound soil mass and the ESB rings. To this end, the geological structure of the test soil had to utilize reflection symmetry with respect to the mid-transverse vertical plane of the ESB. Common geological formations in nature exhibiting lateral inhomogeneities are often sediment-filled valleys of various shapes and aspect ratios; other possibilities include fault sites and cut-and-fill embankments. To simplify the test configuration while retaining the essential components of the problem, a profile consisting of three uniform equivoluminal blocks of sand in the long ESB direction was assembled, with a stiffness contrast between the central block and its neighbors. This configuration guaranteed a degree of lateral stiffness gradation, symmetry and feasibility of construction.

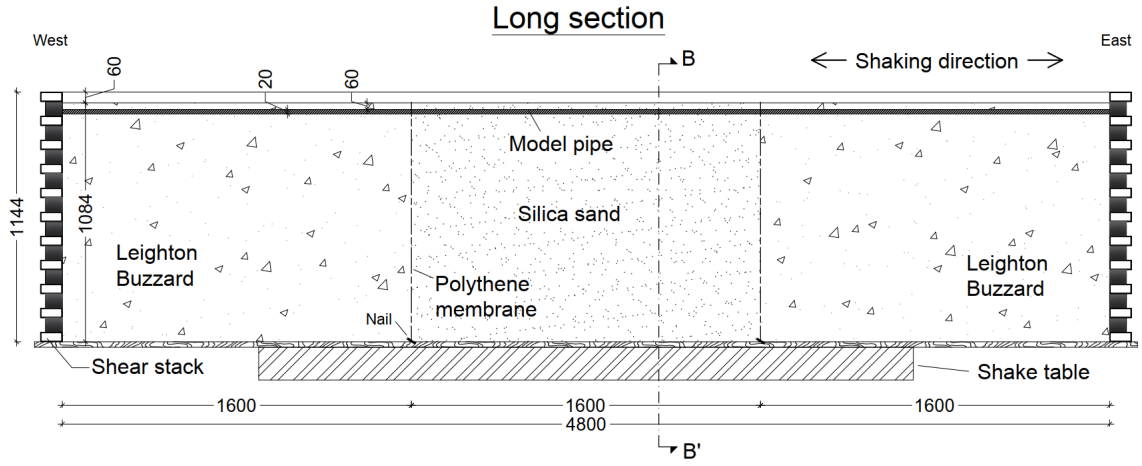

Two dry sand grades were used to form the 3-block profile: Leighton Buzzard sand fraction B (LBB) and Silica Sand (SS). The first is an uncemented medium-coarse sand with rounded grains and well-documented properties (Cavallaro et al. 1992; Stroud 1971) and was readily available in the laboratory. The second consists of uniform fine particles and was procured for the purposes of the experiment. Index data for these sands obtained by sieve analysis are reported in Table 1. SS was on delivery found to contain 2.2% water by weight, but this was judged too low to affect the drainage conditions. The target was to prepare a dense-loose-dense configuration by filling the side blocks with LBB and the

middle one with SS, as illustrated in Fig. 2. By manipulating soil density and in light of its stress-dependency, soil stiffness could be controlled indirectly. More details on sand deposition are provided in the 'Specimen preparation' section.

Scaling laws

Following the line of reasoning developed in Wood et al. 2002, a set of first-order similarity laws were adopted to establish a valid connection between prototype and model, where not all physical quantities obey dimensional analysis principles simultaneously. Like in many 1-g geotechnical models, physical quantities chosen as independent were acceleration (by definition), length, mass density and material stiffness. Scaling was dictated, on one hand, by the reduction of the prototype dimensions, which had to be reasonably large to accommodate lateral variations in soil properties in a realistic way. Given the ESB length, the linear scale for length was decided to be $n \geq 30$ (amounting to a full-scale length not smaller than 30×4.8 = 144 m) to ensure adequate representation of the spatial extent of the problem. The final value chosen was $n = 45$. On the other hand, a constraint inevitably enforced by the simultaneous reduction in the pipe dimensions was the market availability of very thin sections. For the convenience of having the same geomaterial in prototype and model, the scale factor for density was unity. Based on the observation that the small-strain shear modulus of sands, G_o, is related to the mean effective confining stress, σ'_m, through a power law, empirically expressed as $G_o \propto (\sigma'_m)^{0.5}$ (Hardin and Drnevich 1972; Seed and Idriss 1970; Ishihara 1996), the scale factors for all relevant variables were derived in Table 2.

A modified version of the Transitgas pipeline crossing Switzerland was selected as the prototype — the original was used in the numerical study by Psyrras et al. 2019. Its section was redesigned for a lower operating pressure according to a typical safety factor, keeping the same diameter and steel grade, in order to obtain a higher D/t ratio. The resulting pipe characteristics were $D = 900\ mm$; $t = 8.7\ mm$; $D/t \approx 103$; $h = 1.5\ m$; $P/P_y = 0.57$; $SF = 1.75$; $E = 200\ GPa$; $\sigma_y = 448\ MPa$ (h being the burial depth to crown; $P_y = 2\sigma_y t/D$ the yield pressure; SF the safety factor).

The authors' original goal was to experimentally observe plastic buckling effects in the model pipe under test conditions, as predicted numerically in Psyrras et al. (2019). To achieve this in a consistent

126 manner, the scaled pipe should simultaneously obey similitude laws for parameters governing the mode
127 of buckling and the under-pressure collapse axial load, namely D/t ratio, h/D ratio, internal pressure
128 and the plastic material properties, if one ignores the role of geometric imperfections (Yun and
129 Kyriakides 1990).
130 An additional important requirement at model scale would be a minimum pipe anchorage length to
131 allow mobilization of the downscaled collapse load of the model pipe section from the induced frictional
132 stresses at the soil-pipe interface. This length is straightforward to determine analytically given the
133 Coulomb friction force per unit length at the centerline and the target collapse load. An iterative design
134 process was undertaken to find a suitable pipe section in the market to satisfy all, or nearly all, the above
135 conditions. This approach proved troublesome though as it required extremely thin metal alloy tube
136 sections ($t < 0.2$ mm) that no supplier could provide. As a result, it was decided to restrict the model
137 pipe deformation in the elastic range and use a section that approximately retains *secant* stiffness
138 similarity to the protype. Fig. 3 illustrates this idea; the nominal axial stress-axial deformation paths
139 computed from FE shell analysis for the prototype pipe are plotted for various levels of soil confinement
140 and imperfection amplitudes, and the limit loads are identified. A secant elastic modulus $E_{sec}^{(p)}$ is
141 calculated corresponding to the point of collapse at full scale, and the model scale analogue $E_{sec}^{(m)}$ is
142 deduced according to the adopted scaling rule (Fig. 3). If the actual elastic modulus of the model
143 material approximates $E_{sec}^{(m)}$, a reasonable similarity in material stiffness is preserved. As can be
144 observed, the estimated scaled secant modulus $E_{sec,n=45}^{(m)}$ for $n = 45$ approaches the typical range of
145 values for plastics; thus, unplasticized Polyvinyl Chloride (uPVC) was selected as the model pipe
146 material having an experimentally determined elastic modulus of about 2.1 GPa. Model pipe properties
147 are presented in Table 3.

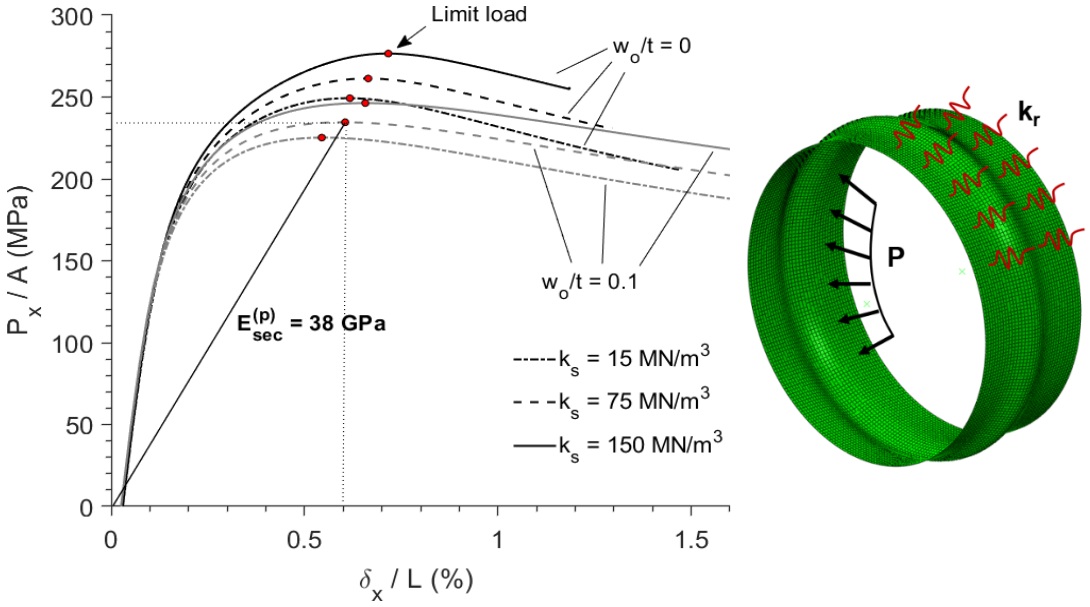

148

149 Care was further taken to preserve dimensionless ratios controlling the pipe response. Because the
150 expected deformation mode of the pipe is alternating compression-extension, the relative soil-pipe axial
151 stiffness is a critical factor. This can be quantified by considering the axial flexibilities of an arbitrarily
152 long straight pipe, clamped at one end, and of an equivalent solid soil bar of equal length and diameter,
153 under uniaxial strain conditions. Then, the *soil-to-pipe* axial flexibility ratio is expressed as (ADD
154 REFERENCE)

$$F_a = 4\,\frac{t}{D}\frac{E_p}{E_s}\frac{(1-\nu_p)(1+\nu_s)(1-2\nu_s)}{(1-\nu_s)(1+\nu_p)(1-2\nu_p)} \tag{1}$$

155 where E_s, E_p and ν_s, ν_p are the elastic moduli and Poisson's ratios of the soil and the pipe material,
156 respectively. Another influencing parameter is the stiffness contrast between the different soil regimes,
157 which may be correlated to the achieved density contrast ρ_{LLB}/ρ_{SS} between the two sands; the latter
158 ratio is preserved from model to prototype at any rate. Note that D/t cannot be preserved, but it is
159 rendered irrelevant since the model pipe response was designed to be elastic, without elastic buckling
160 being a concern. The ratio h/D was handled by the length scaling factor, while a separate dimensionless
161 ratio for internal pressure need not be considered since the effect of pressure was already accounted for
162 in $E_{sec}^{(m)}$. In evaluating grain size effects, the criterion $D/d_{50} \geq 50$ (d_{50}: median grain size) is tested for
163 the two sands (Fioravante 2002). Fine-grained SS passes the test by a margin ($D/d_{50} = 141$), with
164 LBB failing closely ($D/d_{50} = 32$).

Specimen preparation

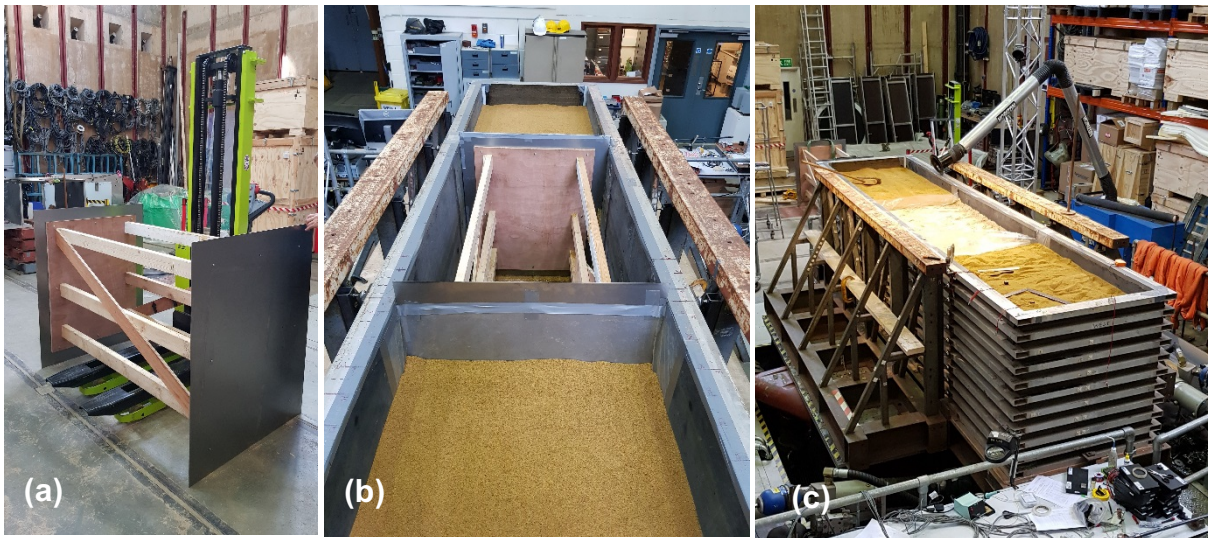

The ESB was securely bolted on the shake table and shaken lengthways. Installation of falsework in the ESB was necessary to partition the three soil blocks throughout the pouring process. In order to maintain a level of density control on the sand blocks, an "inverse" staged construction solution was opted for to facilitate independent compaction of the blocks. A small-scale earth retaining wall system consisting of steel sheets and timber studs was designed and built to temporarily retain the side LBB blocks and permit their compaction before SS was poured in the middle (Fig. 4a). The construction sequence was as follows: the retaining structure was first placed in the ESB and restrained by timber guides; 208-liter drums filled with LBB were crane-lifted above the ESB top and LBB was poured in 10~15 cm layers in the side blocks, up to a target pipe bed elevation of 1005 mm (Fig. 4b). After each pouring, LBB was compacted by persistent low amplitude white noise table vibration, as well as by hand, using custom tamping tools; deposition of SS in the mid-block followed again in layers, combined with gradual uplift of the retaining structure until its complete removal; SS was only slightly compacted and leveled (Fig. 4c); the pipeline specimen was then laid, the sensing instruments were installed and finally the backfill soil was poured, spread and gently leveled to avoid sensor damage or dislocation. The final free surface elevation was 1085 mm, leaving an embedment depth to pipe crown of roughly 60 mm. This violated the prototype h/D ratio of 1.67 but was necessary to ensure a sufficient degree of confinement since the uppermost sand layers were unavoidably very loose. For LBB, the achieved mass density was calculated at 1.63 Mg/m^3 for the bed layer and 1.49 Mg/m^3 for the backfill, while for SS it was 1.40

186 Mg/m^3 for the bed and 1.37 Mg/m^3 for the backfill. A reason why a higher density state for LBB was
187 not achieved as in other tests (e.g., Taylor and Crewe 1996) may be that some local disturbances were
188 induced in the soil while pulling up the retaining structure.
189 Partly on practical grounds, the pipe ends were left unrestrained. This is the most favorable of two
190 extreme conditions in terms of axial strain, the other being clamping one or both pipe ends. The real
191 condition lies in-between these two extremes, as the spatial continuation of the pipeline requires a finite
192 axial stiffness (and force) at the pipe ends.

193 ***Instrumentation***

194 Monitoring the deformation profile in the model pipe at multiple locations was an ideal application for
195 the use of state-of-the-art fiber optic sensors. Two identical Draw Tower Grating (DTG®) chains were
196 custom-ordered; these are spliceless, high-strength FBG cables of ultra-small diameter (125μm)
197 produced by drawing the optical fiber concurrently with inscribing the gratings. As shown in Fig. 5b,
198 cables C1 and C3 were attached to the crown and invert of the pipe, respectively, to monitor the total
199 longitudinal strains. Each one came with 25 strain sensors in a symmetrical configuration having a
200 biased distribution towards the soil block borders. Bonding of the cables on uPVC was achieved using
201 strong instant adhesive. The DTG cables were connected to a Micron Optics interrogator to acquire and
202 process the data. A second identical pipe specimen equipped with two horizontal arrays of resistance
203 strain gauges was also buried in a distance from the basic specimen to evaluate the accuracy of the FBG
204 measurements. A comparison is presented in Psyrras et al. (2019b), showing generally a very good
205 match between the measured strains.
206 Linear, high output acceleration transducers were also deployed to record accelerations in the shaking
207 direction at free-field, table and ESB top. A total of 13 free-field accelerometers were encapsulated in
208 miniature plastic boxes with artificially roughened external faces (via sand adhesion) to maximize
209 friction; 11 of them were aligned parallel to the pipe centerline and two of them were embedded deeper
210 to help extract estimates of the induced shear strains, as shown in Fig. 5a. One of the instruments was
211 secured to the shake table to measure the table motion and another at the third-from-the-top ring to help
212 evaluate the soil-ESB coupling. All deployed transducers are summarized in Table 4.

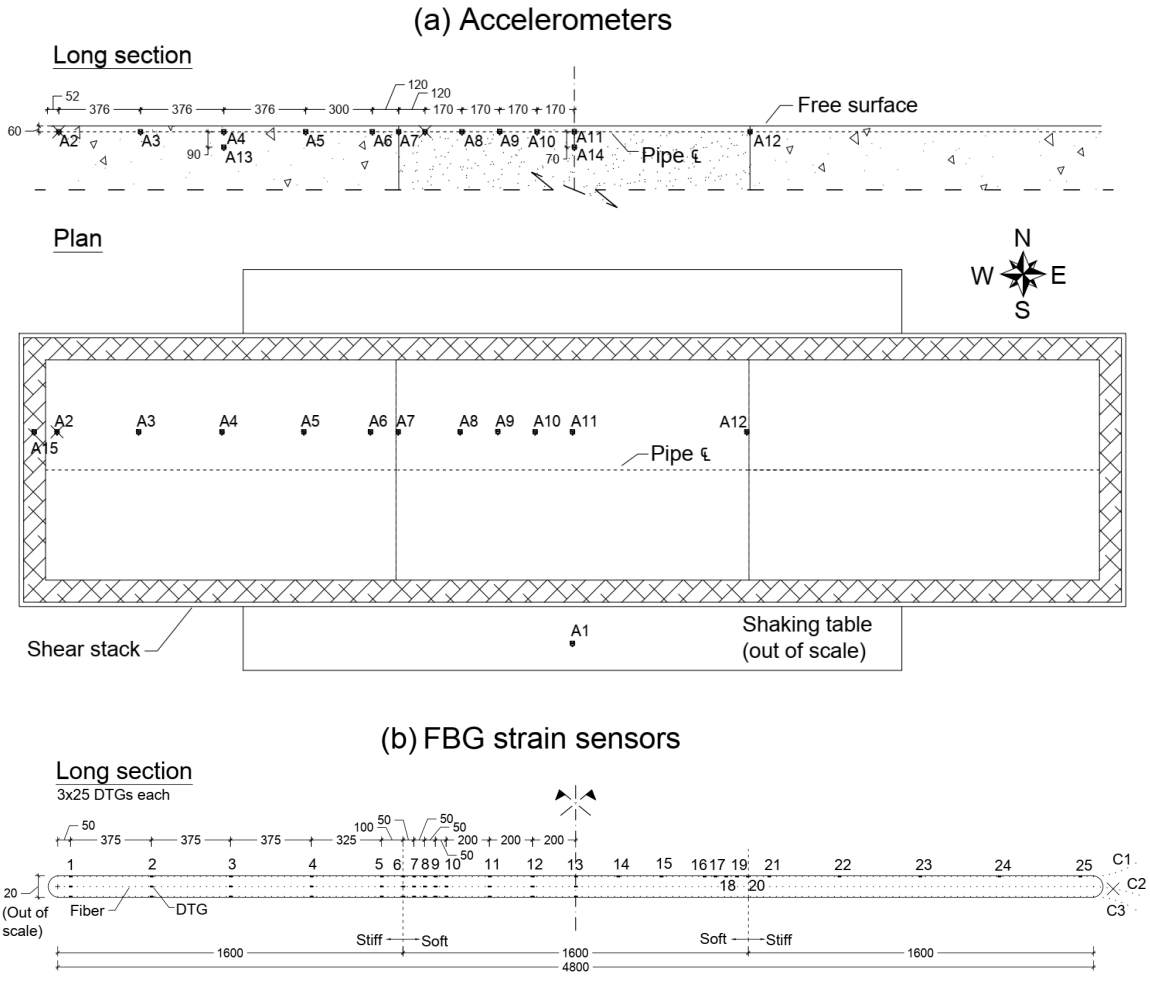

Testing protocol

Gaussian white noise with RMS amplitude of 0.02g was imposed as horizontal table excitation strategically throughout the core testing sequence in an attempt to identify the modal characteristics of the system. The seismic platform was first shaken with modulated harmonics ("sine dwells") at frequencies in the range 8.7-85.0 Hz, equivalent to a range of 0.5-5.0 Hz at full scale, and acceleration amplitudes increasing from 0.01g to 0.1g. At each intensity level, motions were applied from the highest to the lowest frequency to delay unavoidable dilation and contraction effects (Crewe et al. 1998). The time histories of a typical white noise signal and a sine dwell are depicted in Fig. 6.

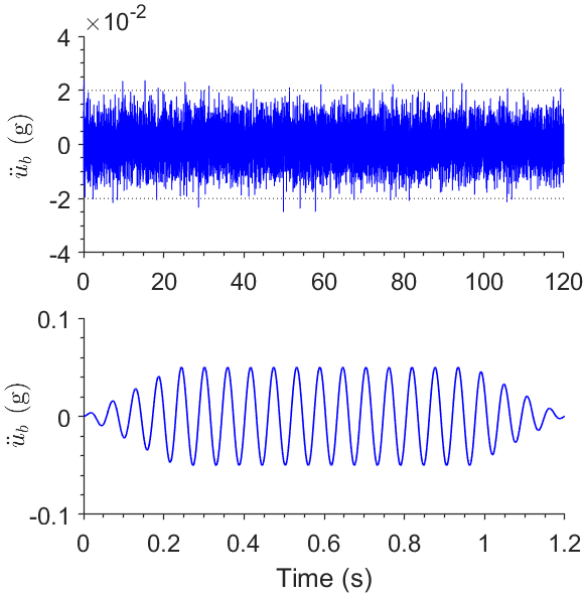

The second phase of the shaking protocol comprised a set of broadband signals in the form of time-compressed versions of recorded strong ground motions, with peak accelerations from 0.06g to 0.49g. Since time was to be compressed by a factor of 0.06, a significant portion of the frequency content of these motions was unavoidably shifted substantially higher (>50 Hz). However, this had implications on the ability of the loaded table to reproduce these high-frequency motions, given that (i) it is a complex hydraulic-mechanical system whose response to input is determined by a nonlinear transfer function and (ii) it exhibits a cut-off frequency that drops significantly with increasing payload. Normally, an iterative approach is taken to match the realized table motion to the target one; due to the risk of sample disturbance and stiffness deterioration under strong excitations, this was not done here, but rather a suite of pre-matched, deconvoluted motions from a previous testing program SERENA (Fiorentino et al. 2019) were used along with some unmatched target motions, whose frequency spectrum was scaled up by a factor of 8.7 instead of the target 17.4. Table 5 lists the properties of these ground motions.

Test results

Data processing

The first operation performed on all raw signals acquired was removal of the mean; where a residual response was observable, only the initial ordinate offset of the signal was subtracted. To convert voltage fluctuations to time-histories of the desired physical parameters, the calibration factors listed in Table 4 were used (λ stands for light wavelength). For soil acceleration histories except the random noise

response, de-noising was achieved using a wavelet transform scheme by soft-thresholding (Donoho 1995); the 'db8' (8^{th} order) wavelet belonging to the Daubechies wavelets family was adopted as basis. This approach was found more effective in reducing noise in seismic signals than the standard band-pass filters requiring specification of cut-off frequencies (Chanerley and Alexander 2007), and was particularly suitable herein because displacement histories were to be derived by time-integration. Raw Fourier Amplitude Spectra (FAS) of acceleration histories were smoothed by passing them three times through a moving average filter with a 49-sample smoothing width; this ensured "smooth ratios" of less than 0.2, sufficient to minimize distortion of the peak heights and bandwidths (O'Haver 2018).

Modal identification

Frequency-Response Functions (FRF) were constructed by computing the FAS of free-field acceleration response histories to random noise input, and then dividing by the FAS of the table input (station A1). FRFs at recording stations A4 (LBB) and A11 (SS) are plotted in Fig. 7 for three cases: before the testing sequence begins, after shaking at 0.1g and in the end of the sequence. It is seen that the responses at both A4 and A11 are predominantly amplified at the same frequency (about 37 Hz for case 1); this confirms the coupled behavior of the sand blocks. FRFs at A11 give a second higher peak amplification at about 56 Hz, which suggests a stiffer middle deposit despite its looser state; this may be explained by the sub-angular shape of SS grains. The resonant frequency of the system drops — moderately— with excitation level to 34.3 Hz, as does maximum amplification. The half-power bandwidth method was used to extract soil internal damping estimates from the FRF low-end peaks. Fig. 8a plots these estimates as a function of the maximum table PGA recorded in the sequence history; evidently, there is a general but inconsistent upward trend across all recordings, from a minimum of 3.1% up to a maximum of 5.7%, with SS exhibiting higher dissipative action. However, it is acknowledged that the derived values might not be reliable due to the strongly spiked shape of the spectra and the associated dependence of the method on the employed smoothing operation. In contrast, Pitilakis et al. (2008) and Chidichimo et al. (2014) measured damping ratios for LBB in excess of 10%. It is not straightforward to obtain estimates of the shear wave velocities V_s^{LB} and V_s^{SS} of the two sands using the expression $V_s = 4 \times f_n \times h$ for horizontally layered deposits. Instead, an attempt was made to approximate these parameters in an average sense from the arrival times of the first incident wave in

the recorded signals at surface, providing also statistical variance of the observations in terms of the standard error of the sample mean. These results are presented in Fig. 8b, where one can identify an initial densification phase for both sands up to 0.05g, and a subsequent non-linear softening phase at higher table accelerations, which is more pronounced for the initially denser LBB. The reduction in mean V_s from the low-strain to the final state is 24% and 10% for LBB and SS, respectively, and the mean stiffness contrast $\overline{V_s^{SS}/V_s^{LBB}}$ achieved at final state is 1.3. Note that, for low table PGAs (<0.05g), no clear peaks were detectable in the acceleration signals, hence the large variability in derived V_s.

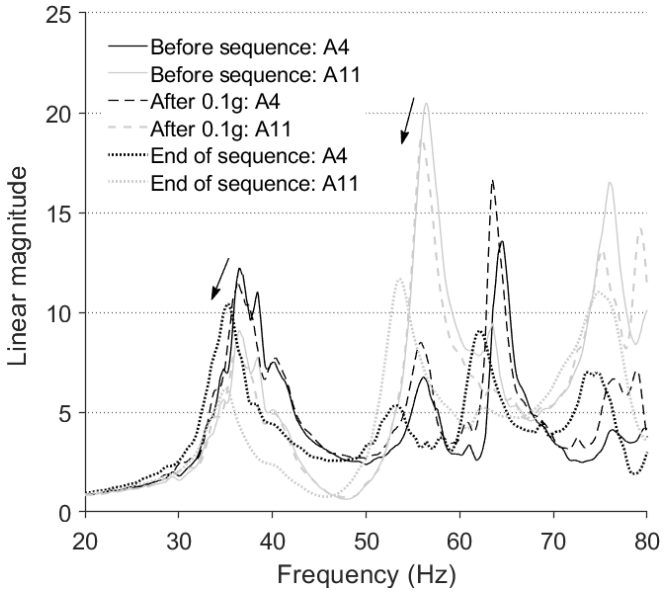

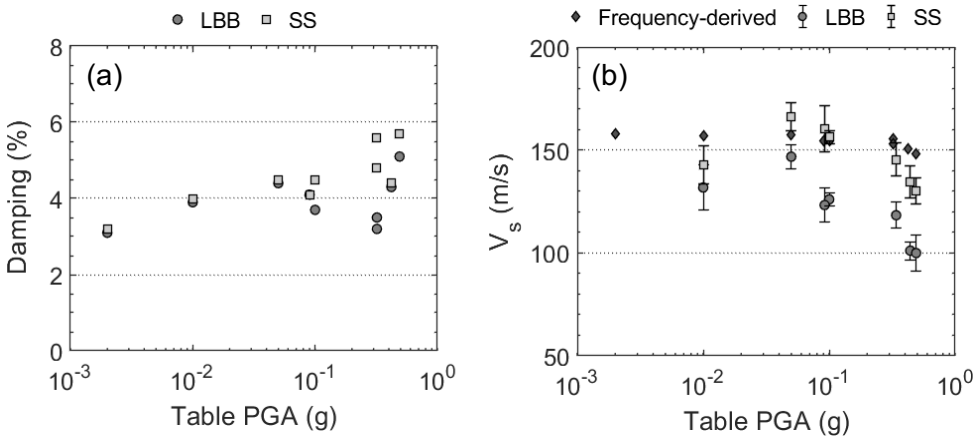

Harmonic excitations

Results for the first phase of single-frequency excitations are reported in this section. Primary outputs obtained are the soil accelerations and pipeline bending strains; derived output includes displacements, axial strains, shear strains and stresses of the soil, and axial strains of the pipeline. Where peak

magnitudes are more of interest, unfiltered results are presented to retain the original character of the measurements.

Fig. 9 plots filtered soil acceleration histories as recorded by sensors A1 (table), A4 and A11 for different harmonic tests — a description of each test is supplied in Table 6. At a loading frequency close to the resonant frequency of ~ 36 Hz (Test H06), horizontal surface motion is amplified by both sands, more strongly by LBB, as shear waves propagate upwards through the soil mass. The degree of amplification depends on the ratio ($\omega_f/\omega_{N,eq}$), where ω_f is the forcing frequency and $\omega_{N,eq}$ is a resonant frequency of a soil block determined by the FRFs of Fig. 7, with zero or negative amplification being possible as experienced in Tests H08 and H11, respectively. It is noted that erratic behavior is observed in SS in some cases in the form of double peaks (e.g., Test H10), which is possibly related to slipping of the instrument casing in the sand.

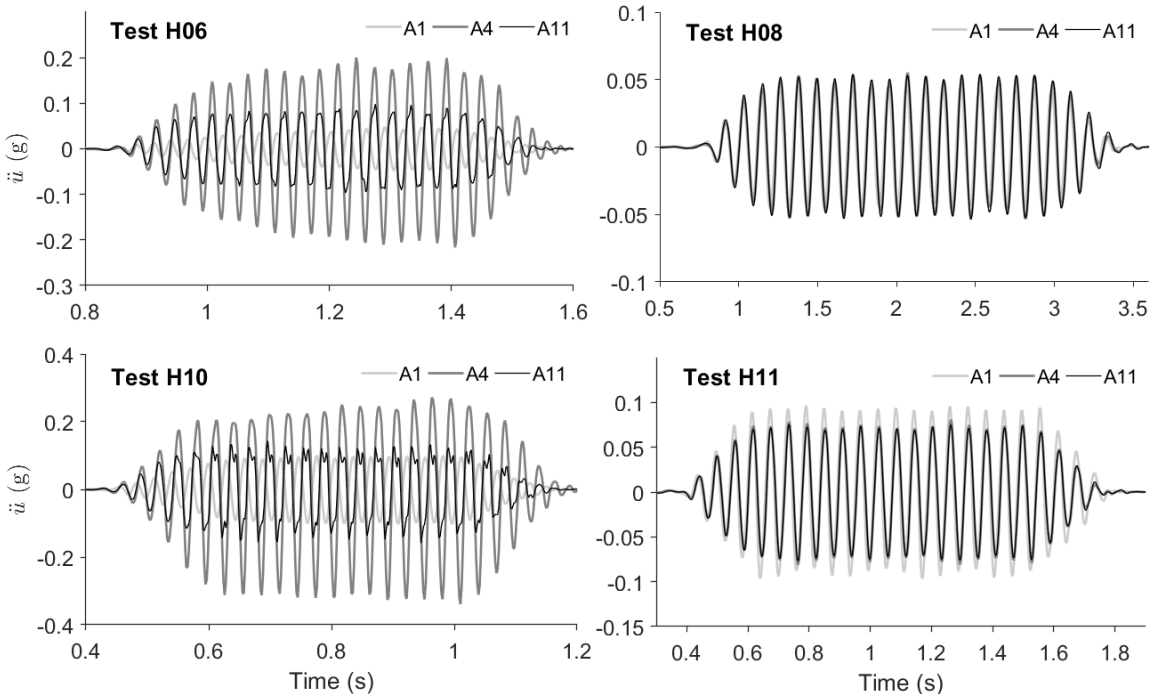

Instantaneous soil acceleration profiles along the recording array A15-A11 are illustrated in Fig. 10. The profiles are extrapolated by reflection beyond the mid-point to cover for the lack of accelerometers in the right half of the setup. For verification, output from sensor A12 is overlaid, showing a good match with the reflected value at the same location. Profiles are plotted for two time instants when a peak and a trough occur. In Test H06, the varying amplification levels in the two soils generate two fairly flat responses across each soil domain, in reasonable agreement with analytical soil amplification studies

(Gelagoti et al. 2010; Psyrras et al. 2019). This behavior results in a relative horizontal motion at the block interfaces, which produces axial normal strain in the soil as shown in the following. On the other hand, surface accelerations are uniform across all blocks in Test H08, in consistency with Fig. 9. Note that sensor A2 was found to be dysfunctional while A11 had undergone unwanted tilting after embedment and for this reason its output was discarded.

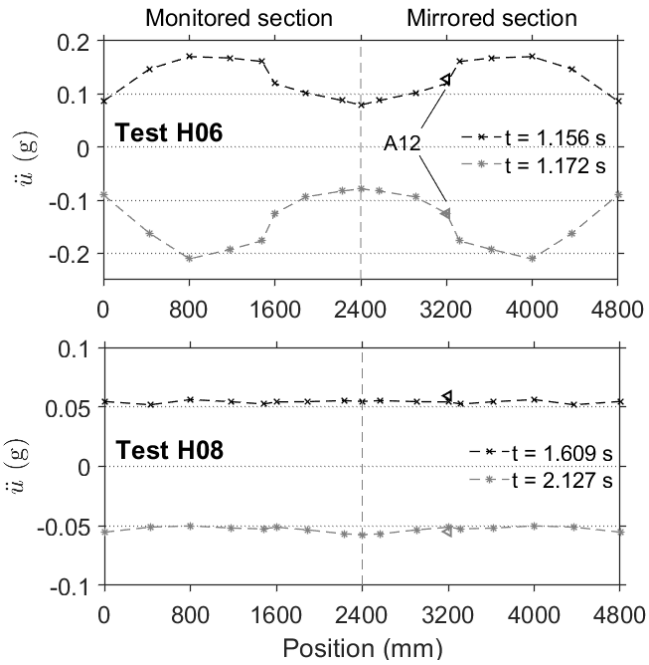

Fig. 11a displays the *total* longitudinal pipeline strains as tracked by the crown and invert optic fibers. As anticipated, the shapes of the profiles are antisymmetric with respect to the mid-point, exhibiting alternating compression-extension at the soil interfaces, depending on the motion direction. Trends also agree very well with analytical studies (e.g. Psyrras et al. 2019). The strain distributions of the crown and invert are very similar, suggesting that bending in the pipe is generally negligible. To get the axial strain profiles, the arithmetic mean of the total strains at the extreme fibers of the tube section $(\varepsilon_C + \varepsilon_I)/2$ suffices, as long as the pipe remains elastic and the neutral axis coincides with the centerline. The axial strains in this first loading phase show mild deviation (< 20%) from the total strains, indicating fairly small in-plane bending effects.

Moreover, to provide a picture of the axial strain transmissibility from soil to pipe, a crude calculation of soil axial strains ε_s at the recording stations was performed using a 2nd-order finite-difference approximation given by Equation 2:

$$\varepsilon_s(x_i) = \frac{(u_{i+1} - u_i)\,\dfrac{x_i - x_{i-1}}{x_{i+1} - x_i} + (u_i - u_{i-1})\,\dfrac{x_{i+1} - x_i}{x_i - x_{i-1}}}{x_{i+1} - x_{i-1}} \quad (2)$$

where u_i is the soil horizontal displacement at station i, computed by double integration of measured acceleration, and x_i is the horizontal coordinate of station i. Fig. 11b shows the near-surface axial strain profiles for Test H06, taken at the same time instants as in Fig. 11a. The distributions resemble the ones measured in the pipe, with magnitudes at the spike being significantly larger; about 50% of the soil strain is seen to be 'transferred' to the pipe in this case, an indication that some interface sliding has occurred.

To gain further insight into the hysteretic response of soil, shear stress-strain loops were developed according to the procedure outlined in Brennan et al. (2005), using the recordings from the two vertical arrays A4-A13 and A11-A14. According to Fig. 12, LBB undergoes much larger shear strains (up to 0.06% in Test H10) than SS for the same excitation level. The loops are fairly stable, but nonlinearity is hardly discernible; the slopes through the origin equating to secant shear moduli confirm that SS is a stiffer sand than LBB. Also, the deeper the station, the stiffer the sand as one would expect.

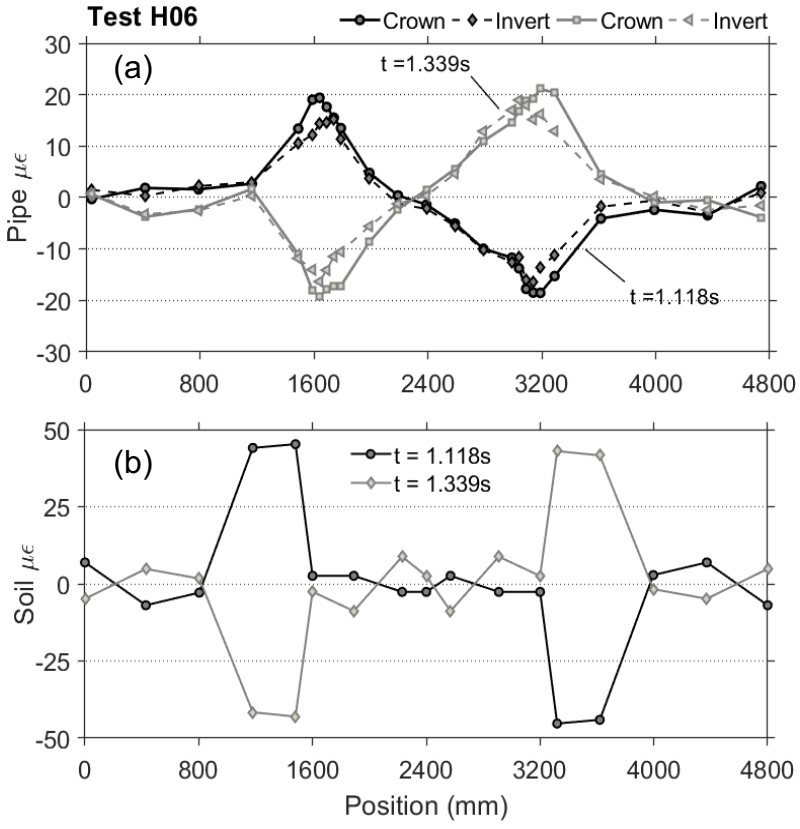

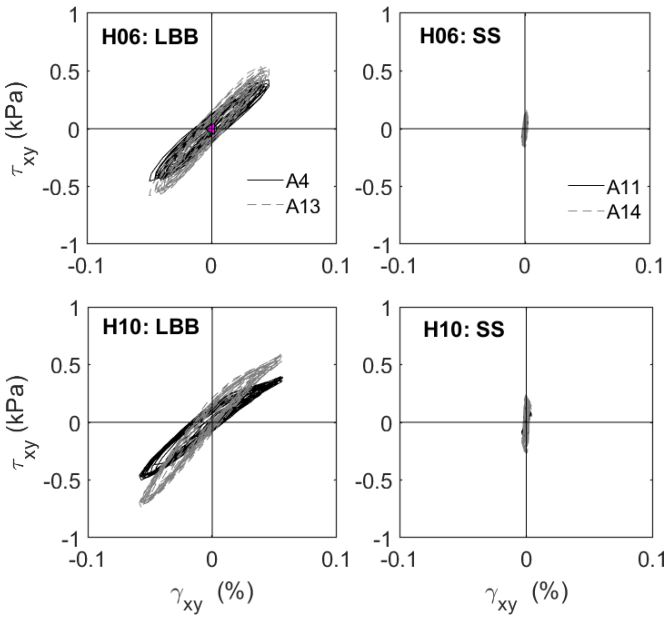

335

336 ***Broadband excitations***

337 Along similar lines, select results obtained for broadband table input are presented here. In the top row
338 of Fig. 13, representative acceleration responses for the two sands as recorded by the mid-block
339 instruments A4 and A11 are plotted for cases SM06 and SM08. Again, variable surface motion
340 amplification is understood to impose increased relative axial displacements on the pipeline. The bottom
341 row of Fig. 13 shows the axial pipe strains calculated at stations falling on the block interfaces, for the
342 same loading cases. By close inspection, it is seen that the peak strains are nearly in phase with the soil
343 acceleration peaks. Axial strain histories at stations 6 and 20 are rough reflections of each other about
344 the x-axis, which again confirms the alternating compressive-extensional deformation mode in the pipe
345 close to the block interfaces. Moreover, in the cases shown, residual stresses and (elastic) strains are
346 observed post-shaking due to residual ground deformations that alter the configuration of the pipe.
347 Critical tensile and compressive strain profiles for the same test cases are presented in Fig. 14. The
348 profiles in solid line refer to axial strain; dashed lines show actual recorded total strain at the extreme
349 fibers. It is evident that absolute peaks are substantially increased compared to the harmonic tests, up
350 to 66 $\mu\varepsilon$ for axial strain and 140 $\mu\varepsilon$ for total strain. Interestingly, bending strains are becoming significant
351 as revealed by the disparity between total and axial strains; their proportion of total strains amounts to
352 51%, as can be seen in Fig. 15. The reason for this is that higher dilatational modes are more strongly
353 excited in the ground; these modes involve vertical components of motion, manifesting close to the

block interfaces, that bend the pipeline. Table 6 summarizes all directly measured and derived peak response parameters: soil acceleration, soil horizontal normal (axial) strain, soil shear strain, pipe total longitudinal strain, pipe axial tensile and compressive strain.

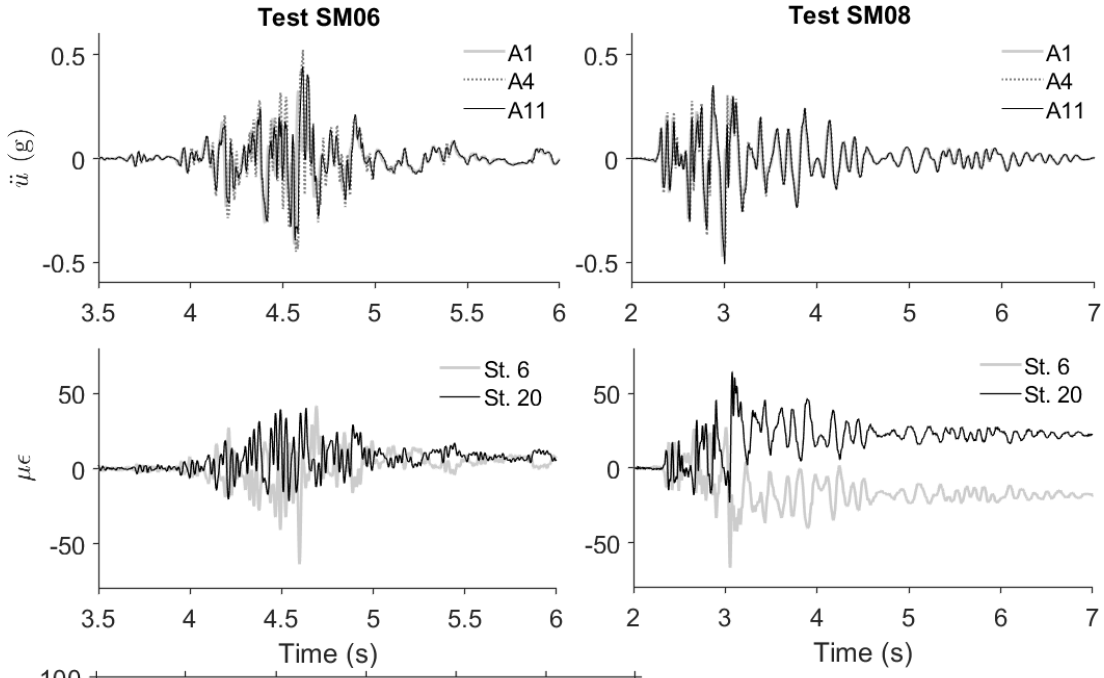

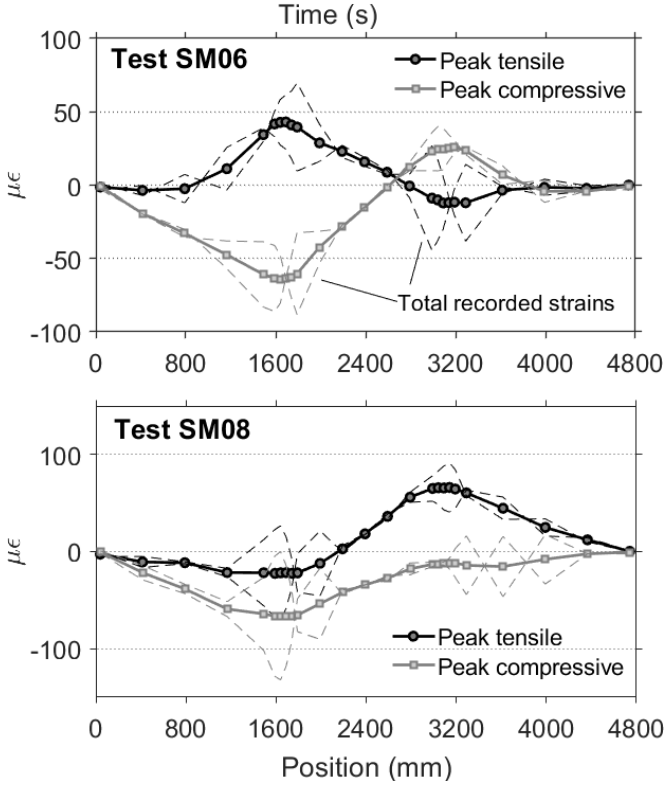

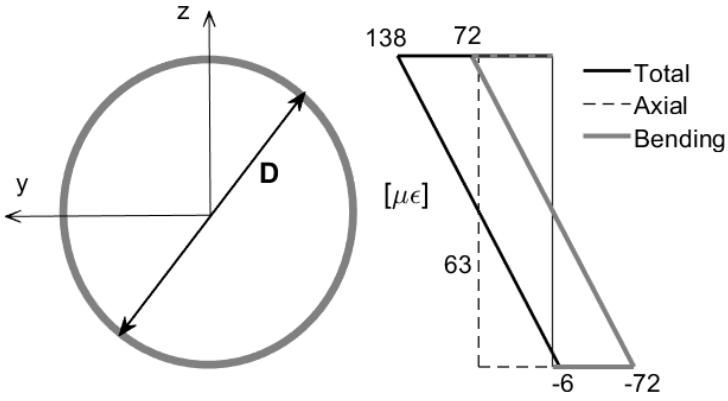

Numerical validation of test results

ABAQUS (Dassault Systèmes 2014) and Opensees (McKenna et al. 2010) were employed to simulate these experimental tests with the finite element method. Given the irregularity in geometry and inhomogeneity in material properties of the geotechnical specimen, 2-D continuum elements were used in the first place to verify the experimentally observed free-field response at the surface. Salient details of the experimental assembly were included in the model, such as the lateral boundaries of the ESB and their contact response with the soil mass.

Eigenvalue extraction

The modal and material characteristics of the system as of Test WN4 were considered as reference to compare against. Only the soil and components of the ESB were included in the eigenvalue analysis. A structured mesh with plane-strain finite elements was created to discretize six distinct subdomains in the test soil (Fig. 16), accounting for the difference in measured densities between pipe bed layer (ρ) and backfill (ρ') for both sands. Shear moduli were determined as $G = \rho\, V_s^2$ and a constant Poisson's ratio $\nu = 1/3$ was assumed across all subdomains. To couple the motion between the two ESB ends, tie constraints were enforced at all ring levels. The interaction of test soil and ESB at their interface was modelled using a finite-sliding, surface-to-surface contact discretization, assuming an interface COF equal to the as-measured internal COF of LBB, $\tan(32.6°) = 0.64$, in view of the sand-roughened internal ESB surfaces. Using mean observed V_s values from Fig. 8b, the numerical model was found to be more flexible in its first mode, with the corresponding natural frequency underestimating the experimentally observed frequency of 35.8 Hz by ~10%. Fig. 17 shows the first four eigenmodes; the

lowest eigenfrequency is associated with a coupled shear-dilatational mode of vibration, as a result of the non-uniform shear stiffness of the soil. Higher modes involve more dominant flexural and vertical modes, both symmetric and antisymmetric ones. By comparison with Fig. 7, it is seen that the numerical model captures well the second and fourth eigenfrequency as well.

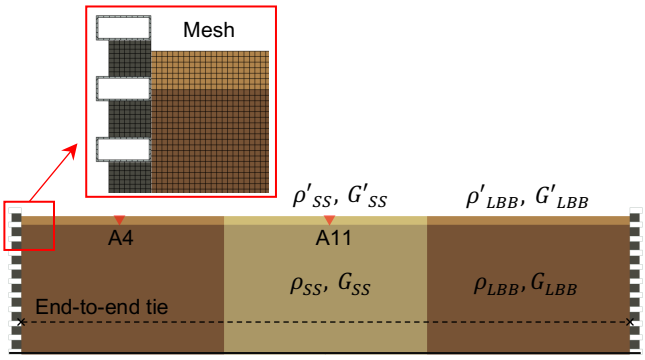

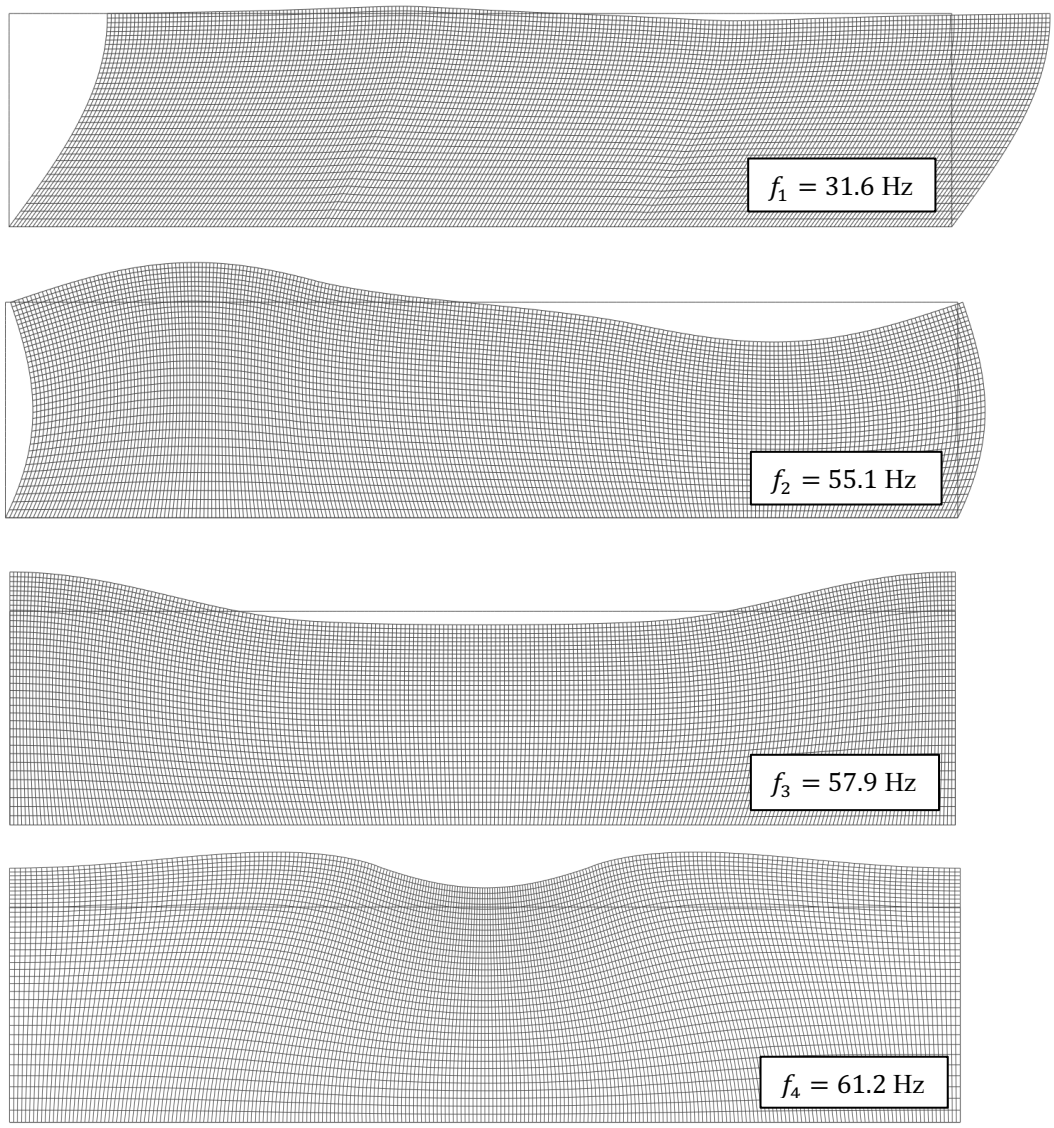

Transient response

To reproduce numerically the time-varying response of the soil and pipe to base excitation for Test H10, the two-step approach adopted in Papadopoulos et al. (2017) was employed ~~tested~~. In the first step, the 2-D soil-ESB model in Fig. 16 was solved for the realized table motion and the horizontal and vertical acceleration response histories were extracted at soil nodal points along the pipe centerline. The soil behavior was assumed as damped linearly elastic and an effective stiffness was determined from the mean observed V_s for the two sands. Viscous damping of the Rayleigh type was introduced using target damping ratios as identified for the respective excitation level in Fig. 8a.

Ignoring kinematic and inertial interaction effects, a separate, bi-directional, multi-support-excitation model of the pipeline idealized as an assembly of 2-D Euler-Bernoulli beams was developed in Opensees in the second step, where the frictional and transverse vertical SPI was represented by non-linear spring elements. A fine element mesh was created to match the spatial resolution of the strain sensors. Spring parameters were evaluated according to standard expressions proposed by the ALA (American Society of Civil Engineers 2001), with the axial mobilizing relative displacement computed from separate FE pipe pull-out analysis as 2×10^{-5} m and 3×10^{-5} m for LB and SS, respectively. The ground spring nodes were subjected to the previously obtained horizontal and vertical free-field displacements at pipe bed level.

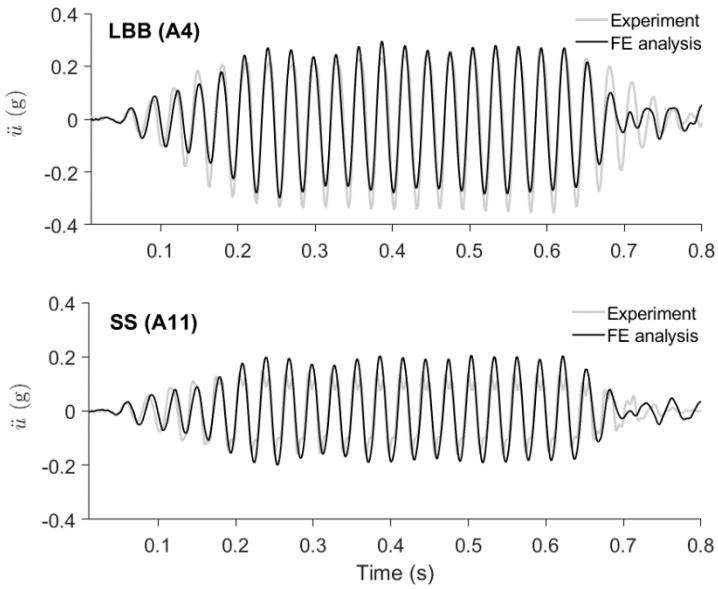

As illustrated in Fig. 18, the steady-state response of LBB sand compares favorably with the recorded response at A4, less a minor time lag. The average peak-to-peak discrepancy in the constant-amplitude

410 window is ~5% and ~17% in the positive and negative direction, respectively, the difference being due
411 to the lack of x-symmetry in the experimental response. Similarly, the match for SS is better in the
412 negative than in the positive direction. Here, the effect of the double peaks, briefly discussed earlier,
413 becomes obvious as it leads to a markedly larger discrepancy in the positive direction.
414 Shown in Fig. 19 are the axial strain histories at stations 6 and 20 as computed from analysis and as
415 measured from test. For station 20, the results show differences in the strain magnitudes, though this is
416 exaggerated by the fact that the experimental response is drifting away from the baseline. Ignoring the
417 drift, the model underpredicts the pipe strains by an average 55%. The overall shapes are in good
418 agreement. For station 6, the match appears better, if one again ignores the drift. To trace the source of
419 these discrepancies, an attempt was made to back-calculate the time-varying frictional force profile
420 generated along the pipe specimen and compare against the frictional resistance used for the axial
421 springs. The general equation of motion of a continuous Euler-Bernoulli beam on dynamic non-linear
422 Winkler foundation for axial excitation was used, given by

423 $$\rho_p A \frac{\partial^2 u_p}{\partial t^2} - E_p A \frac{\partial^2 u_p}{\partial x^2} = t_u \qquad (3)$$

424 where $u_p = u_p(x,t)$ is the absolute axial pipe displacement and $t_u = t_u(x,t)$ is the friction force per
425 unit length. Using the recorded pipe strain profiles and safely assuming that the inertial term is
426 negligible (if the recorded soil acceleration is used in place of pipe acceleration, this term is two orders
427 of magnitude smaller than the axial restoring force), the envelopes of t_u were calculated at each strain
428 monitoring point for four different test outputs. Fig. 20 plots these envelopes normalized with respect
429 to the Coulomb frictional resistance $t_{u,ALA} = \mu\gamma' h(\frac{1+K_o}{2})\pi D$. Where the envelopes do not cross the
430 dotted horizontal line (=ALA), it means that $t_{u,ALA}$ captures reliably the friction response. It can be seen
431 that for the low-intensity test HM06, the envelopes lie below the ALA line almost everywhere. In stark
432 contrast, the friction envelopes for test HM10 exceed the ALA resistance by a factor of 9.5 within the
433 ground stiffness transition zones. This indicates that the soil conditions developing in these zones offer
434 additional t_u to the pipe, allowing increased axial strains to develop, as measured. In particular, as
435 shown in the foregoing, the soil in these zones undergoes compression-extension cycles; during
436 compression, the confining stress in the soil increases near the soil-pipe interface, leading to an increase

in the contact stress, hence an increase in t_u locally. This increase in t_u is evident in the other two tests too, although not as sharp. The main reason why t_u is so much larger in HM10 is that the test soil in this case experiences near-resonance effects, which entails stronger amplification of the lateral displacements, thus more excessive compression.

Overall, the comparison for the soil response is judged acceptable, permitting to say that the computer model developed lends credence to the test results. For the response of a pipe buried in a laterally inhomogeneous soil, more refined SPI models are essential to capture the cyclic variation in frictional resistance with the changing confining conditions at inhomogeneity features, as the ALA springs were developed for pipelines in laterally uniform soil.

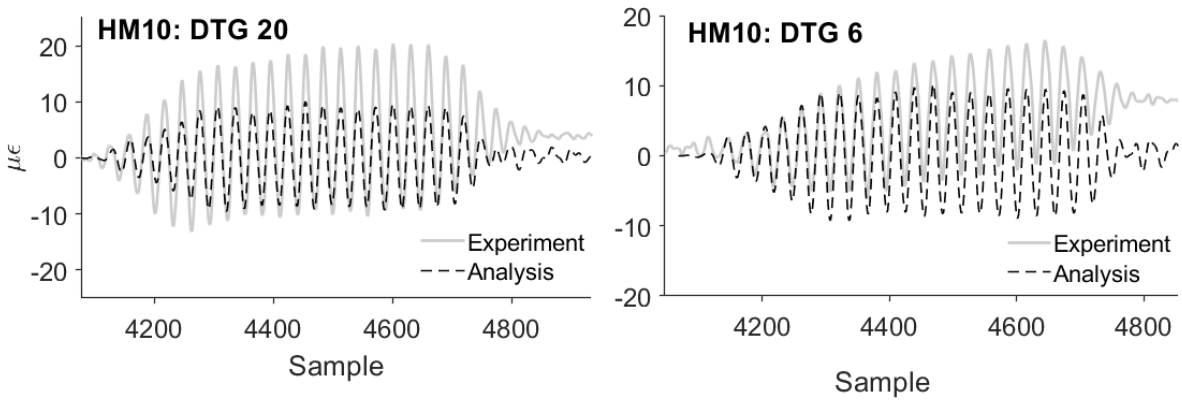

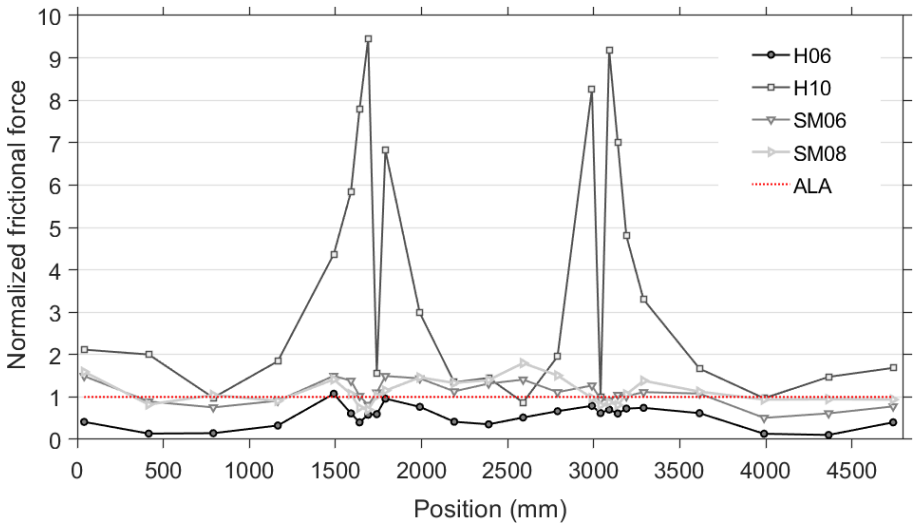

Discussion

When the peak pipe response obtained from the experiment is extrapolated to full-scale using the similitude laws outlined above, the peak total strain ~~becomes~~ is on the order of ~~0.1%~~ 10^{-3} (~~by~~ after division by the scale factor for strain of 0.149), which is nearly half the yield strain of the prototype

steel and nearly 1/6 of the limit strain corresponding to the plastic buckling load, shown in Fig. 3. This result reveals a significant margin of safety for the prototype pipeline; however, it shows a non-negligible reduction of the safety factor against buckling. Accordingly, it would be unwise to assume that axial strain concentrations generated at the soil boundaries would never result in shell buckling. If a more unfavorable combination of parameters were in place, such as a higher interface COF —as normally is the case for the steel-sand interface— and a larger soil stiffness contrast, the axial and bending strains developing in the pipe inside the transition zone may become substantially larger. Note that the ratio $\overline{V_s^{SS}/V_s^{LBB}}$ in this study varied from an initial 1.1, to 1.3 post-shaking, that is fairly low ratios.

From another standpoint, this series of tests demonstrates the benefit of a low interface COF as a means of reducing the dynamic axial loads transferred from ground to pipe during ground shaking. For comparison, using the simple SPI model presented above, the peak total strain in the pipe for the seismic input of Test HM10 and a uniform COF $\mu = 0.8$ across both sands is computed at 58 $\mu\varepsilon$, nearly three times larger than for $\mu = 0.23$. Given that the pipe is constructed along an engineered trench, this mitigating effect could be achieved in different ways, such as by using smooth, low-friction pipe coatings, or installing layers of geosynthetic wrapping around the pipe to trigger axial slip at these interfaces (Honegger et al. 2002).

It is also worth noting that the testing sequence was performed in an uninterrupted fashion, assuming independent seismic events. However, the initially 'perfect' soil state and soil-pipe contact state was disturbed after the first strong table motions. This may have led to a gradual reduction ~~of the~~ in in-situ COF, hence placing a cap on the stress transfer to the pipe in subsequent tests. Unfortunately, there was no capability to measure the level of contact pressure at the pipe walls in this study. The implication is that, in the scenario of a single strong earthquake event where no loss of interface contact has previously occurred, the frictional stresses will likely induce larger axial strains in the pipeline than measured ~~in the last tests~~ here. Further experimental work could shed more light on these aspects by deploying additional sensors, such as tactile pressure transducers and displacement transducers to measure settlements.

Concluding remarks

New data from 1-g shake table tests of a 1:45 model of an onshore transmission gas pipeline embedded in a laterally non-homogeneous site, were presented and discussed. The experiment physically modelled the coupled dynamic response of the site and the pipeline under a set of uniaxial harmonic excitations and modified earthquake records applied in the pipeline direction. Three blocks made up from two types of dry sand were cast in a special 4.8-m-long, 1.2-m-tall, 1.0-m-wide soil container to form a symmetric test site with three zones of different soil stiffness, i.e. soft-stiff-soft, and the pipeline specimen was laid in and covered. Pipeline strain measurements were obtained from two chains of fiber optic sensors bonded on the pipeline specimen. The test data were validated against finite element models. The main findings are summarized below:

- The state of deformation in the system is similar to the one reported in other studies dealing with ground stiffness transitions, the difference being that in this study the stiffness pattern in the soil was reversed. It was confirmed that alternating compression-extension zones develop in the pipeline very close to the soil block boundaries, following the ground deformation pattern, while non-shear ground deformation remains negligible far from those interfaces. This anti-symmetric strain pattern is a result of the varying horizontal free-field motion amplification and vertical ground vibrations associated primarily with higher modes, which mobilize increased frictional stresses on the pipe walls.
- From the harmonic motion sequence, it was found that~~,~~ for a given inhomogeneous site, pipeline strain magnitudes are governed by resonance effects on the site response. Peak strains were monitored for $\omega_f/\omega_{N,eq} \approx 1$ for two different table excitation levels, 0.05g and 0.1g. Tests for stronger input motions showed that the induced strains increased notably also with surface PGA, reaching values ~~of~~ as high as 140 $\mu\varepsilon$ for PGA = 0.57g.
- Bending strains in the pipeline became considerable at stronger excitations, amounting up to 50% of the total strains. This is an indication of vertical-flexural ground modes becoming active at higher exciting frequencies, forcing the pipe to bend near the stiffness transition zones.

- A relatively simple plane-strain finite element model was successful in reproducing the recorded site surface response; however, using a beam-on-springs model with ALA spring parameters proved inadequate to predict satisfactorily the pipe strain response, especially close to the stiffness transitions zones. This is attributed mainly to the inability of the axial springs to capture the large increment in frictional resistance offered by the increased confinement in these zones, which allows transfer of additional axial stresses to the pipe.
- Results show that the prototype would accommodate the scaled-up strains of 0.1% without yielding. Nevertheless, subtle variations in configuration, such as a higher soil stiffness ratio and a higher interface COF, may potentially incur a more critical response in the pipeline.

The above conclusions are subject to specific assumptions made in the employed test setup and general limitations associated with 1-g testing. Most prominently, the test model is adequate to first order and the extrapolation of the pipe response is to performed in respect to the limit point of the full-scale pipe. The pipe model ends were left unrestrained; this set of boundary conditions generally leads to reduced axial distress due to friction forces compared to a pipe model with clamped ends. Lastly, the test-to-test change of the soil-pipe contact conditions could not be monitored.

Data Availability Statement

Some or all data, models, or code generated or used during the study are available from the corresponding author by request. Items included are the raw experimental data, the signal processing scripts, and the finite-element models used for reproduction of the tests.

Acknowledgements

This work was funded by the Horizon 2020 Program of the European Commission through grant MSCA-RISE-2015-691213-EXCHANGE-Risk. The first author also expresses his gratitude to the Engineering and Physical Sciences Research Council for financially supporting his doctoral studies (grant no.: EP/M507994/1). The invaluable assistance of all technical staff involved in the project is acknowledged, with special thanks to L. de Leeuw for carrying out the direct shear tests. Finally, the authors thank Dr G. Tsinidis, Dr D. Karamitros, Dr T. Horseman and Dr N. Alexander for their contribution through critical discussions of this work.

References

Akiyoshi, T., and Fuchida, K. (1988). “Seismic Response of Pipeline Systems Buried in Dipping Soil Layers.” *Proc. 9th World Conference on Earthquake Engineering*, Tokyo-Kyoto, Japan.

American Society of Civil Engineers. (2001). *Guideline for the Design of Buried Steel Pipe*.

Ando, H., Sato, S., and Takagi, N. (1992). “Seismic Observation of a Pipeline Buried at the Heterogeneous Ground.” *Proceedings of the Tenth World Conference on Earthquake Engineering*.

Brennan, A. J., Thusyanthan, N. I., and Madabhushi, S. P. (2005). “Evaluation of Shear Modulus and Damping in Dynamic Centrifuge Tests.” *Journal of Geotechnical and Geoenvironmental Engineering*, 131(12), 1488–1497.

Cavallaro, A., Maugeri, M., and Mazzarella, R. (1992). “Static and Dynamic Properties of Leighton Buzzard Sand From Laboratory Tests.” (1), 1–6.

Chanerley, A. A., and Alexander, N. A. (2007). “Correcting data from an unknown accelerometer using recursive least squares and wavelet de-noising.” *Computers and Structures*, 85(21–22), 1679–1692.

Chen, W. W., Shih, B., Chen, Y.-C., Hung, J.-H., and Hwang, H. H. (2002). “Seismic response of natural gas and water pipelines in the Ji-Ji earthquake.” *Soil Dynamics and Earthquake Engineering*, 22(9–12), 1209–1214.

Chidichimo, A., Cairo, R., Dente, G., Taylor, C. A., and Mylonakis, G. (2014). “1-g Experimental investigation of bi-layer soil response and kinematic pile bending.” *Soil Dynamics and Earthquake Engineering*, Elsevier, 67, 219–232.

Crewe, A. J., Lings, M. L., Taylor, C. A., Yeung, A. C. K., and Andrighetto, R. (1995). “Development of a large flexible shear stack for testing dry sand and simple direct foundations on a shaking table.” *European Seismic Design Practice, Research and Application: Proc. Fifth SECED Conference, Chester UK*, A. S. Elnashai, ed., Balkema, 163–168.

Crewe, A. J., Simonelli, A., and Scotto di Santolo, A. (1998). “Shaking table tests of scale models of gravity retaining walls.” *Seismic Design Practice into the Next Century*, Booth, ed., Balkema, Rotterdam.

Dassault Systèmes. (2014). “ABAQUS.” Dassault Systèmes, Inc., Providence, RI.

Donoho, D. L. (1995). “De-Noising by Soft-Thresholding.” *IEEE Transactions on Information Theory*, 41(3), 613–627.

EQE Summary Report. (1995). *The January 17, 1995 Kobe Earthquake*.

Fioravante, V. (2002). “On the shaft friction modelling of non-displacement piles in sand.” *Soils and Foundations*, 42(2), 23–33.

Fiorentino, G., Cengiz, C., De Luca, F., De Benedetti, G., Lolli, F., Dietz, M., Dihoru, L., Lavorato, D., Karamitros, D., Briseghella, B., Isakovic, T., Vrettos, C., Topa Gomes, A., Sextos, A., Mylonakis, G., and Nuti, C. (2019). “Shaking Table Tests on an Integral Abutment Bridge Model: Preliminary Results.” *COMPDYN 2019, 7th International Conference on Computational Methods in Structural Dynamics and Earthquake Engineering*, M. Papadrakakis and M. Fragiadakis, eds.

Gelagoti, F., Kourkoulis, R., Anastasopoulos, I., Tazoh, T., and Gazetas, G. (2010). “Seismic wave propagation in a very soft alluvial valley: Sensitivity to ground-motion details and soil nonlinearity, and generation of a parasitic vertical component.” *Bulletin of the Seismological Society of America*, 100(6), 3035–3054.

Hardin, B. O., and Drnevich, V. P. (1972). “Shear Modulus and Damping in Soils: Design Equations and Curves.” *Soil Mechanics and Foundations Division*, (SM7), 667–692.

Hindy, A., and Novak, M. (1979). “Earthquake response of underground pipelines.” *Earthquake Engineering & Structural Dymamics*, 7, 451–476.

Honegger, D. G., Gailing, R. W., and Nyman, D. J. (2002). “Guidelines for the Seismic Design and Assessment of Natural Gas and Liquid Hydrocarbon Pipelines.”

Housner, G. W., and Jennings, P. C. (1972). “The San Fernando California Earthquake.” *Earthquake Engineeirng and Structural Dynamics*, 1(August 1971), 5–31.

Ishihara, K. (1996). Soil Behaviour in Earthquake Geotechnics, Oxford University Press

Liang, J. (1995). “3-D Seismic Response of Pipelines Through Multiple Soil Media.” *PVP-Vol. 312*, 101–107.

Lings, M. L., and Dietz, M. S. (2004). “An improved direct shear apparatus for sand.” *Géotechnique*, 54(4), 245–256.

Liu, X., and O’Rourke, M. J. (1997). “Seismic Ground Strain at Sites With Variable Subsurface Conditions.” *Computer Methods and Advances in Geomechanics*, J. X. Yuan, ed., A. A. Balkema, Wuhan, 2239–2244.

McKenna, F., Scott, M. H., and Fenves, G. L. (2010). “Nonlinear Finite-Element Analysis Software Architecture Using Object Composition.” *Journal of Computing in Civil Engineering*, American Society of Civil Engineers, 24(1), 95–107.

Nishio, N., Ishita, O., and Tsukamoto, K. (1983). “Model experiments on the behavior of buried pipelines during earthquakes.” *Am. Soc. Mech. Eng., Pressure Vessels Piping Div., (Tech. Rep.) PVP; (United*

States).
Nishio, N., Ukaji, T., and Tsukamoto, K. (1980). "Experimental Studies and Observation of Pipeline Behavior During Earthquakes." *PVP-Vol. 43*, 67–76.
O'Haver, T. (2018). *A Pragmatic Introduction to Signal Processing with applications in scientific measurement*. *University of Maryland at College Park*.
O'Rourke, M. J. (2009). "Wave Propagation Damage to Continuous Pipe." *Technical Council on Lifeline Earthquake Engineering Conference (TCLEE), Oakland, CA, June 28-July 1.*, American Society of Civil Engineers, Reston, VA.
O'Rourke, M. J., and Hmadi, K. El. (1988). "Analysis of continuous buried pipelines for seismic wave effects." *Earthquake Engineering & Structural Dynamics*, 16(6), 917–929.
O'Rourke, M. J., and Liu, X. (1999). *Response of Buried Pipelines Subject to Earthquake Effects*. Buffalo, New York.
O'Rourke, T. D., and Palmer, M. C. (1996). "Earthquake performance of gas transmission pipelines." *Earthquake Spectra*, 12(3), 493–527.
Papadopoulos, S. P., Sextos, A. G., Kwon, O.-S., Gerasimidis, S., and Deodatis, G. (2017). "Impact of spatial variability of earthquake ground motion on seismic demand to natural gas transmission pipelines." *16th World Conference on Earthquake Engineering, Santiago, Chile, 9-13 January.*
Pitilakis, D., Dietz, M., Wood, D. M., Clouteau, D., and Modaressi, A. (2008). "Numerical simulation of dynamic soil-structure interaction in shaking table testing." *Soil Dynamics and Earthquake Engineering*, 28(6), 453–467.
Psyrras, N. K., and Sextos, A. G. (2017). "Safety of buried steel natural gas pipelines under earthquake-induced ground shaking : a review." *Soil Dynamics and Earthquake Engineering*, Elsevier Ltd, 106(March), 254–277.
Psyrras, N., Kwon, O., Gerasimidis, S., and Sextos, A. (2019a). "Can a buried gas pipeline experience local buckling during earthquake ground shaking?" *Soil Dynamics and Earthquake Engineering*, Elsevier Ltd, 116(October 2018), 511–529.
Psyrras, N., Sextos, A., Crewe, A., Dietz, M., and de Leeuw, L. (2019b). "Shaking table tests of the seismic response of transmission gas pipelines in non-homogeneous soil." *Second International Conference on Natural Hazards and Infrastructure*, G. Gazetas and I. Anastasopoulos, eds., National Technical University of Athens, Chania.
Psyrras, N., Sextos, A. G., Kwon, O.-S., and Gerasimidis, S. (2018). "Safety factors of buried steel natural gas pipelines under spatially variable earthquake ground motion." *11th National Conference on Earthquake Engineering*, Earthquake Engineering Research Institute, Los Angeles, California.
Sakurai, A., and Takanashi, T. (1969). "Dynamic Stresses of Underground Pipelines During Earthquakes." *Proceed. of 4th World Conf. on Earthq. Engng.*, Santiago, Chile, 81.
Seed, H. B., and Idriss, I. M. (1970). *Soil moduli and damping factors for dynamic response analyses*. Berkeley, Calif. : College of Engineering, University of California.
Shinozuka, M., and Koike, T. (1979). *Estimation of Structural Strains in Underground Lifeline Pipes*.
Stroud, M. . (1971). "The behaviour of sand at low stress levels in the simple-shear apparatus (Doctoral thesis)." University of Cambridge.
Taylor, C., and Crewe, A. (1996). "Shaking table tests of simple direct foundations." *Proc. 11th World Conference on Earthquake …*.
Timoshenko, S. P., and Gere, J. M. (1961). *Theory of Elastic Stability*. Engineering Series, McGraw-Hill.
Trautmann, C. H., and O'Rourke, T. D. (1985). "Lateral force-displacement response of buried pipe." *Journal of Geotechnical Engineering*, 111(9), 1077–1092.
Tsinidis, G., Di Sarno, L., Sextos, A., Psyrras, N., and Furtner, P. (2018). "On the numerical simulation of the response of gas pipelines under compression." *Ninth International Conference on Advances in Steel Structures (ICASS)*.
Wood, D. M., Crewe, A. J., and Taylor, C. A. (2002). "Shaking table testing of geotechnical models." *International Journal of Physical Modelling in Geotechnics 1*.
Yu, H., Zhang, Z., Chen, J., Bobet, A., Zhao, M., and Yuan, Y. (2018). "Analytical solution for longitudinal seismic response of tunnel liners with sharp stiffness transition." *Tunnelling and Underground Space Technology*, Elsevier, 77(March), 103–114.
Yun, H., and Kyriakides, S. (1990). "On the beam and shell modes of buckling of buried pipelines." *Soil Dynamics and Earthquake Engineering*, 9(4), 179–193.

Tables and Figure Captions

Table 1. Index properties for the sands used in the test

Grade	Void ratio		Grain size (mm)			Uniformity coefficient	Grain shape	Source
	Min	Max	d_{10}	d_{50}	d_{60}	C_u		
Leighton Buzzard B	0.49	0.78	0.450	0.620	0.70	1.56	Rounded	Lings and Dietz (2004)
Silica Sand	0.67	0.93	0.094	0.141	0.156	1.66	Sub-angular	Supplier; in-house testing

Table 2. 1-g scale factors employed in this study; variables in italics taken as independent

Variable	Scale factor (prototype-to-model)	Value for $n = 45$
Length	$1/n$	0.022
Density	1	1
Stiffness	$1/n^{0.5}$	0.149
Acceleration	1	1
Stress/Pressure	$1/n$	0.022
Strain	$1/n^{0.5}$	0.149
Displacement	$1/n^{1.5}$	0.003
Velocity	$1/n^{0.75}$	0.058
Time	$1/n^{0.75}$	0.058
Frequency	$n^{0.75}$	17.37
Wave propagation velocity	$1/n^{0.25}$	0.386
Force	$1/n^3$	0.000011

Table 3. Model pipe properties

Parameter	Unit	Value
Elastic modulus, E_p	MPa	2100
Poisson ratio, ν_p	-	0.4
Mass density, ρ_p	Mg/m^3	1.36
External diameter, D	mm	20
Wall thickness, t	mm	1.5
Axial rigidity, E_pA	kN	261.5
Interface COF against LBB*	-	0.23
Interface COF against SS†	-	0.27

*, † Measured at a normal pressure of 10 kPa

Table 4. Details of transducers deployed in the test

Type	Number	Measured parameter	Characteristics	Calibration
Accelerometer SETRA 141A	14	Horizontal free-field and base acceleration	High output linear sensor Operating frequency: 0-3000 Hz Low transverse sensitivity 0.012g/g	1 g/V
Draw Tower Gratings (DTG®) by FBGS Technologies	3×25	Pipeline bending and axial strain	Bare FBG strain sensors in low bend loss fiber; reflectivity >15% Interrogator: Micron Optics si255 (f_{sample} = 1000 Hz)	$1.2/(\Delta\lambda/\lambda)$

Table 5. Target ground motions used in this study

ID	Location and year	Station	Magnitude M_w	PGA (g)	Mean period at 1:1 (s)	Time scale factor
1	Italy 2017	AMT	5.4	0.09	0.40	0.2
2	Italy 2016	CSC	5.4	0.06	0.48	0.2
3	Italy 1998	SELE	5.0	0.09	0.36	0.2
4	Italy 2016	AMT	6.2	0.34	0.62	0.2
5	Italy 2016	AMT	6.5	0.44	0.48	0.2
6	Kocaeli 1999	Yarimca	7.6	0.35	1.34	0.1
7	Lefkada 2003	No. 1	6.2	0.42	0.48	0.1

Table 6. Recorded and derived peak values of response parameters of interest for all test cases

Test ID	Description	Target table PGA (g)	Peak soil $\ddot{u}_g$ (g)	Peak pipe ε_{tot} ($\mu\varepsilon$)	Max pipe ε_a ($\mu\varepsilon$)	Min pipe ε_a ($\mu\varepsilon$)	Peak soil ε_a ($\mu\varepsilon$)	Peak soil γ_{xy} (%)
WN1	White noise	0.02						
H01	SD* 0.01g 85Hz	0.01	0.064	10	7	-8	11	0.003
H02	SD 0.01g 34Hz	0.01	0.069	9.7	8	-8	20.6	0.01
H03	SD 0.01g 17Hz	0.01	0.02	8	6	-6	10	0.01
H04	SD 0.01g 8.7Hz	0.01	0.028	8	7	-6	27	0.05
WN2	White noise	0.02						
H05	SD 0.05g 85Hz	0.05	0.23	48	25	-10	22	0.01
H06	SD 0.05g 34Hz	0.05	0.23	26	23	-22	88	0.05
H07	SD 0.05g 17Hz	0.05	0.05	8	8	-7	21	0.04
H08	SD 0.05g 8.7Hz	0.05	0.07	9	8	-8	28	0.3
WN3	White noise	0.02						
H09	SD 0.1g 85Hz	0.1	0.29	13	12	-10	40	0.02
H10	SD 0.1g 34Hz	0.1	0.36	54	32	-25	155	0.08
H11	SD 0.1g 17Hz	0.1	0.11	12	10	-9	45	0.08
H12	SD 0.1g 8.7Hz	0.1	0.14	23	12	-14	80	0.8
WN4	White noise	0.02						
SM01	GM 1	0.068	0.14	13	11	-11	35	0.23
SM02	GM 2	0.063	0.19	19	16	-17	58	0.41
SM03	GM 3	0.0925	0.09	27	14	-7	31	0.24
WN5	White noise	0.02						
SM05	GM 4	0.34	0.42	62	37	-46	332	3
WN7	White noise	0.02						
SM06	GM 5	0.42	0.64	96	78	-72	930	2.3
WN8	White noise	0.02						
SM07	GM 6	0.35	0.44	68	39	-46	248	3.9
SM08	GM 7	0.49	0.57	140	73	-87	821	4.2
WN9	White noise	0.02						
H13	SD 0.3g 34Hz	0.3	0.58	89	54	-46	407	0.16

* SD = sine dwell; GM = ground motion

Figure 1. (a) The 6-DOF shaking table at the EQUALS research facility at University of Bristol; (b)-(c) aspects of the large ESB used.

Figure 2. Long section of the as-built test setup showing the geometry of the soil profile and the model pipe (all units in mm).

Figure 3. Shell axial load – axial shortening responses for the adopted prototype pipeline for various moduli of subgrade reaction k_s and normalized wall imperfection amplitudes w_o/t. In the FE model, deformation plasticity is employed for steel constitutive behavior; the radial elastic soil springs k_r are calculated using k_s and nodal influence areas; the imperfection is axisymmetric with a sinusoidal shape and (elastic) half-wavelength estimated as $1.57\sqrt{Rt}$ (Timoshenko and Gere 1961). Drawn is $E_{sec}^{(p)}$ for $k_s = 75\ \mathrm{MN}/m^3$ and $w_o/\mathrm{t} = 0.1$. Using values from Table 2, target $E_{sec,45}^{(m)} = 5.6$ GPa for n = 45.

Figure 4. (a) Purpose-built auxiliary earth-retaining structure; (b) aspect of the filled with LBB sand side blocks during staged soil deposition; (c) the compound soil mass poured in to pipe bed level.

Figure 5. (a) Configuration of acceleration transducers in the soil mass and test rig; (b) configuration of fiber optic cables on the pipeline specimen to monitor axial and bending strains

Figure 6. Typical Gaussian white noise with $\mathrm{PGA_{RMS}} = 0.02$g (top) and sine dwell at f = 17.4 Hz (bottom) used as input motions

Figure 7. Smoothed FRFs, generated from white noise excitation, at surficial recording stations in the LBB and SS blocks, in different phases during the testing sequence; arrows indicate the gradual reduction of modal frequency with shaking intensity

Figure 8. (a) Variation of damping ratios of LBB and SS with table excitation level; (b) Variation of mean shear wave velocities of LBB and SS with table excitation level along with standard mean errors; plotted also is the V_s variation of an equivalent laterally uniform 1-D soil column, determined from knowledge of the measured natural frequencies

Figure 9. Recorded soil acceleration time-histories at surface stations A4 and A11 for different tests

Figure 10. Soil acceleration profiles along the horizontal recording array

Figure 11. (a) Axial profiles of pipeline total longitudinal strains at extreme fibers; (b) axial profiles of soil axial normal strain computed along the accelerometer array

Figure 12. Shear stress–strain loops evaluated at stations A4, A13 (LBB) and A11, A14 (SS) for Tests H06 (0.05g) and H10 (0.1g); averaged measures of shear strain histories between the sensors were used (accurate to 1st order)

Figure 13. Time traces of recorded soil accelerations at surface stations A4, A13 and of axial pipe strains at interface stations 6 and 20, for different broadband table excitations

Figure 14. Critical tensile and compressive axial strain profiles along the pipeline for different broadband table excitations; shown in dashed lines are the recorded total strains at the crown and invert fibers

Figure 15. Section total, axial and bending pipe strains at St. 6, at the time of the critical compressive profile of Test SM08

Figure 16. Finite element model of the ESB-soil system in two dimensions

Figure 17. The first four computed eigenmodes of the ESB-soil system; scaling of deformation is not consistent across modes

Figure 18. Comparison of acceleration response histories in LBB and SS between FE model and the experiment

Figure 19. Comparison of pipe axial strain histories between FE model and the experiment at two monitoring points

Figure 20. Variation of back-calculated frictional force per unit length along the pipeline from different tests, normalized with respect to the frictional resistance recommended by the ALA guideline